ACS APPLIED MATERIALS & INTERFACES

www.acsami.org

Research Article

Ternary Electrochemiluminescence Biosensor Based on DNA Walkers and AuPd Nanomaterials as a Coreaction Accelerator for the Detection of miRNA-141

Qian Wang,[‖] Yaqi Liu,[‖] Xuefeng Wang, Fengyi Wang, Lina Zhang, Shenguang Ge,* and Jinghua Yu

Cite This: *ACS Appl. Mater. Interfaces* 2021, 13, 25783−25791

Read Online

ACCESS | Metrics & More | Article Recommendations | Supporting Information

ABSTRACT: In this study, a ternary electrochemiluminescence (ECL) sensing platform coupled with a multiple signal amplification strategy was proposed for ultrasensitive detection of miRNA-141. The initial signal amplification was achieved via three-dimensional reduced graphene oxide (3D-rGO)@Au nanoparticles (NPs) to form an excellent conductive layer. Then, AuPd NPs as a coreaction accelerator was introduced into the *N*-(4-aminobutyl)-*N*-(ethylisoluminol) (ABEI)−H_2O_2 system to facilitate the transformation from H_2O_2 to excess superoxide anion radicals ($O_2^{\bullet-}$), which further amplified the ECL emission of ABEI, leading to a significant increase of the ECL signal. Meanwhile, in the presence of miRNA-141 and T7 Exonuclease (T7 Exo), the self-assembled DNA swing arm can be driven to walk autonomously. The DNA walker reaction could result in the release of numerous labeled luminophores, which could react to achieve an extremely weak ECL signal. Surprisingly, the established ECL sensor platform for the detection of miRNA-141 demonstrated excellent sensitivity with a low detection limit of 31.9 aM in the concentration range from 100 aM to 1 nM. Consequently, the designed strategy greatly improves the luminous efficiency of the ternary ECL system and provides a special approach for the detection of nucleic acids and biomarkers in clinical and biochemical analysis.

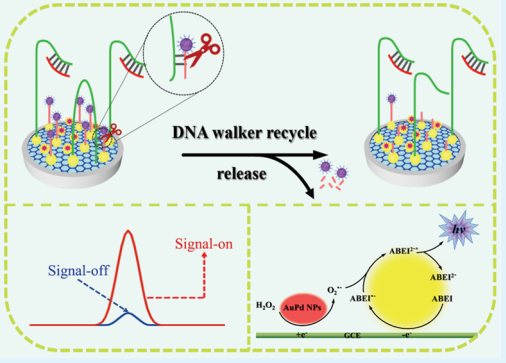

KEYWORDS: *electrochemiluminescence, microRNA-141, three-dimensional reduced graphene oxide@Au nanoparticles, AuPd nanoparticles, DNA walker*

1. INTRODUCTION

MicroRNAs (miRNAs) as an abundant species of single-stranded endogenous noncoding small RNAs[1,2] are unanimously regarded as significant minimally invasive biomarkers.[3−5] Nevertheless, the precise monitoring and quantitative analysis of miRNAs are still full of challenges due to their small volumes, ultralow expression performance, and high homology. Traditional methods for miRNA expression determination, including quantitative real-time reverse transcription-polymerase chain reaction,[6−8] northern blotting,[9−11] and microarray chip,[12−14] have been widely applied. Although new technologies such as surface-enhanced fluorescence,[15] Raman spectroscopy,[16,17] and electrochemistry[18] have been developed for further detection, the implementation of a single technique cannot substantially meet the requirements for ultrasensitive detection of miRNAs at low concentrations. Consequently, utilizing a multistrategy signal amplification protocol to raise the sensitivity and portability of miRNA detection is particularly necessary.

Among various amplification technologies, DNA walkers[19−22] are a particular class of the molecular nanomachines and have drawn tremendous attention due to the cascade signal enhancement characteristics of their autonomous motion.[23,24] As for a classic DNA walker, the target can simulate the biological protein motor to trigger a particular DNA to move along the predesigned DNA tracks automatically and continuously.[25,26] Nevertheless, such nanomachines with specific foot-bonds have limited walking areas, slow reaction dynamics, and complex strand displacement reactions. Therefore, the unfettered DNA walkers[27,28] with multiple walking "legs" on the same substrate were developed by researchers to achieve high-speed walking kinetics and high progression signal processing ability. As a powerful biomagnification technology, an enzyme-assisted cyclic amplification strategy can further improve the target conversion ratio.[29−31] Using the single-enzyme-assisted dual circulation amplification strategy,[32,33] double loop amplification was realized by combining with the DNA walker strand-displacement reaction

Received: March 23, 2021
Accepted: May 6, 2021
Published: May 25, 2021

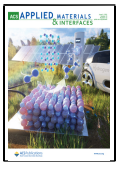

Scheme 1. Schematic Illustration of Synthetic Steps of ABEI@AuPd NPs (A); Schematic Diagram of the Biosensor Based on DNA Nanomachines Walking Freely on Electrodes for the Detection of miRNA-141 (B); and the Possible ECL Mechanism of ABEI@AuPd NPs (C)

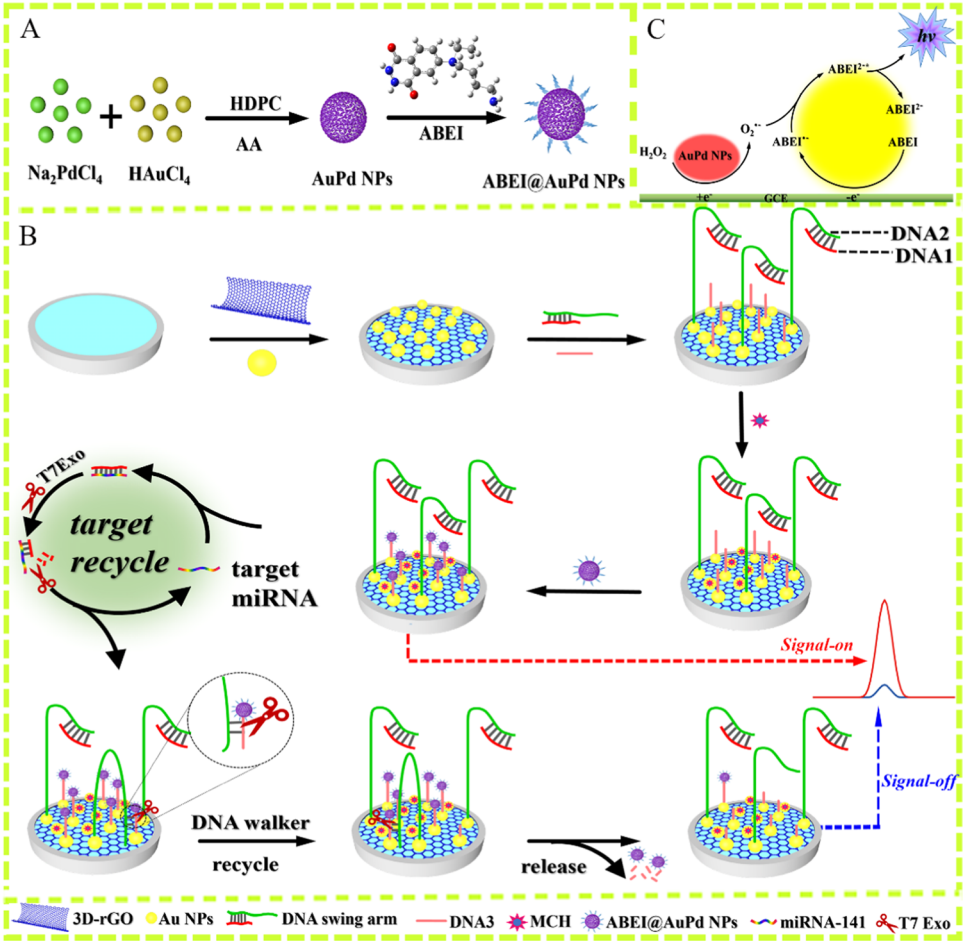

(SDR)[34,35] and T7 Exonuclease (T7 Exo) to avoid the interference reactions and attenuate environmental sensitivity.

Electrochemiluminescence (ECL)[36−39] as a signal amplification strategy has drawn considerable focus in clinical medical examination and drug monitoring owing to its low amplitude limit, high sensitivity, wide linear dynamic range, and controllable reaction process.[40] Relying on the advantages above, numerous reactants with excellent performance have been explored gradually to increase the luminescence quantum efficiency in unit time. *N*-(4-Aminobutyl)-*N*-(ethylisoluminol)[41] (ABEI) has been confirmed to be a novel derivative of luminol, which is more reactive than the prototype and is easier to react with coreactants, leading to stronger ECL.[42−44] To further amplify a signal, a coreaction accelerator was introduced into a luminophore/coreactant system, which could catalyze the coreactant to increase the formation of free radical intermediates for acquiring a higher excited state of the luminophore.[45] As a result of the synergistic effect between the alloying atoms and high refracture index surface, AuPd NPs with extraordinary catalytic performance were selected to construct an ECL ternary system.[46−48]

In this study, combined with T7 Exo-assisted DNA walker cascade amplification and the coreaction emitter boost mechanism, an "on−off" ternary ECL biosensor with multistrategy signal enhancement effect was proposed for ultrasensitive detection of miRNA-141. First, porous spherical AuPd NPs were accurately synthesized and loaded with ABEI to form ABEI@AuPd NPs (Scheme 1A). As shown in Scheme 1B, the 3D-rGO@Au NPs were synthesized and decorated on the bare glassy carbon electrode (GCE) surface to build a high-strength electron transmission channel. Besides, both the DNA swing arm (consisted of DNA1 and DNA2 by complementary chain hybridization to limit the base pairing of DNA2 and DNA3 on the obtained electrode) and the DNA3 were assembled on the GCE through the Au−S bond[49−51] for DNA walker amplification. Then, ABEI@AuPd NPs were labeled at one end of DNA3, which catalyzed H_2O_2 to produce a large amount of $O_2^{\bullet-}$ to form a "signal-on" state of ECL. Nevertheless, when the target of miRNA-141 was incubated on the electrode, the DNA1 hybrided with the miRNA-141 to make up a duplex structure, releasing DNA2 to integrate with DNA3 on the decorated electrode. Meanwhile, with the assistance of T7 Exo, DNA1 in RNA/DNA hybrids was cut into fragments, which led to the releasing of miRNA-141 and binding with other DNA1 to realize the target recovery. Moreover, DNA3-ABEI@AuPd NPs could also be sheared from the electrode interface, and the DNA2 as the swing arm was freely paired up with another DNA3 again to activate the walking processes of the DNA nanomachine. A large number of ABEI were discarded from the electrode surface, and the ECL signal changed to the "signal-off" state. Therefore, the

https://doi.org/10.1021/acsami.1c05368
ACS Appl. Mater. Interfaces 2021, 13, 25783−25791

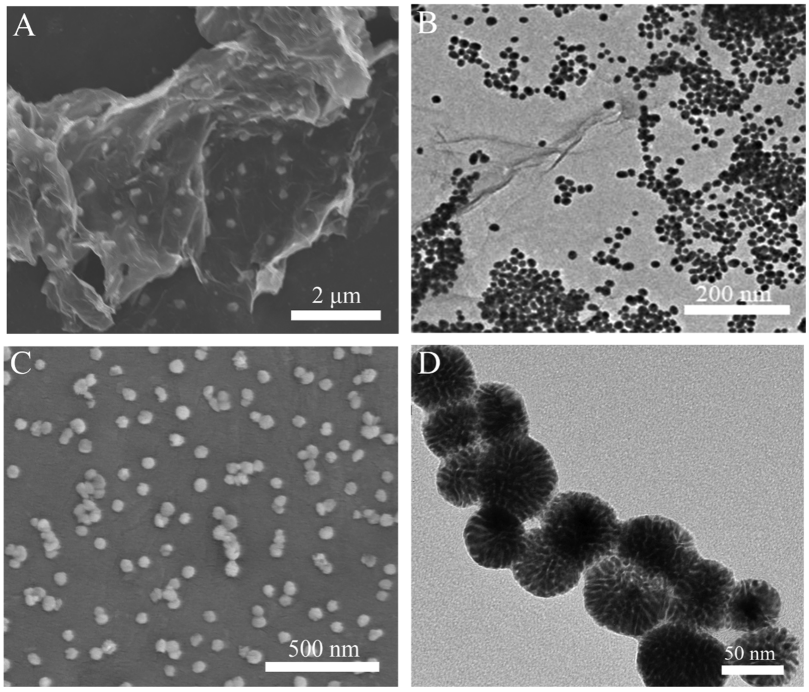

Figure 1. (A, C) SEM images of 3D-rGO@Au NPs and AuPd NPs, respectively. (B, D) TEM images of 3D-rGO@Au NPs and AuPd NPs, respectively.

target could be quantitatively monitored through the real-time response of the ECL signal.

2. EXPERIMENTAL SECTION

2.1. Materials and Apparatus. The materials and apparatus are listed in the Supporting Information.

2.2. Preparation of 3D-rGO@Au NPs. To synthesize 3D-rGO@Au NPs, 4 mg of rGO was dispersed in 50 mL of ultrapure water under sonication and stirring for 5 min; then, 15 mg of $HAuCl_4$ was added slowly to 3D-rGO dispersion with stirring at room temperature. The prepared composite suspension was kept for 30 min to facilitate the interaction of gold ions with the surface of wrinkled graphite. Subsequently, 5 mL of sodium citrate solution (with a sodium citrate to ultrapure water mass ratio of 0.02) was added under magnetic stirring for 30 min. Afterward, the mixed solution was heated to 80 °C and kept for 1 h. Finally, the solution was centrifuged (7000 rpm) and washed with ultrapure water three times to eliminate the unadsorbed free Au NP binding solution formed. The successfully synthesized 3D-rGO@Au NPs were dried in a 60 °C oven for 12 h and protected from light at 4 °C in a refrigerator before use.

2.3. Synthesis of AuPd NPs and ABEI@AuPd NPs. The porous AuPd NPs were constructed by the traditional wet-chemical method with minor optimization. Simply, Na_2PdCl_4 and $HAuCl_4$ as metal sources will undergo a violent oxidation−reduction reaction in the presence of the reducing agent ascorbic acid (AA), and the surfactant chlorohexadecyl pyridine (HDPC) can further enhance the permeability and solubility of active metal ions. The specific process can be depicted as follows: first, 0.8 mL of 10 mM Na_2PdCl_4 and 82 μL of 1% $HAuCl_4$ were uniformly blended under magnetic stirring. Next, 18 mg of HDPC particles was dissolved in 10 mL of ultrapure water and added into the above solution. After evenly mixing, the freshly made AA aqueous solution was poured into the above mixed liquids swiftly while constantly stirring and maintaining the temperature at 35 °C for 3 h. Then, the above solution was centrifuged at 10 000 rpm for 10 min and washed with ultrapure water four times to eliminate the residuum. Finally, the synthesized AuPd NPs were stored in a refrigerator at 4 °C.

The process of the synthesis of ABEI@AuPd NPs can be summed up as follows. First, the 4 mmol/L ABEI solution was formed by directly adding ABEI in 0.1 mol/L NaOH. After the obtained AuPd NPs were ultrasonically dispersed for 2 h, 500 μL of the ABEI stock solution was added and stirred for 12 h. The mixed ABEI@AuPd NPs were presented by the interface reaction between AuPd NPs and $-NH_2$ groups of ABEI, washed with ultrapure water to eliminate the unlocked ABEI. Finally, the obtained ABEI@AuPd NPs were resuspended in 5 mL of ultrapure water at 4 °C for the subsequent process of the experiment.

2.4. Fabrication of the Biosensor. Prior to modification, the GCE was disposed using 1.0 and 0.05 μm of alumina slurry to a mirrorlike burnished finish. Then, 10 μL of 3D-rGO@Au NP solution was dripped onto the as-prepared bare GCE and dried in air. Subsequently, the mixture of 5 μM DNA1 oligonucleotide and 2.5 μM DNA2 oligonucleotide was doped and diluted with 92.5 μL of 1 × TE. Then, the corresponding solution was warmed to 95 °C for 5 min and annealed to room temperature. At this time, the complex structure known as the DNA swing arm was successfully synthesized. Then, 10 μL of the above solution and 10 μL of 100 μM DNA3 were muddled in 80 μL of Tris−HCl buffer to obtain the stock solution. After incubation with 10 μL of the stock solution for 12 h at 4 °C, the electrode was immersed in 10 μL of 1.0 mM 6-mercapto-1-hexanol (MCH) for 40 min to secure the active sites. Finally, ABEI@AuPd NPs were modified on the electrode, and the biosensor was obtained.

2.5. ECL Measurement Procedure. For ECL detection of target miRNA, 100 U/mL T7 Exo and various concentrations of miRNA-141 were successively assembled into an as-fabricated DNA nanomachine for 3 h at 25 °C. After removing the unbound residues with 1 × TE buffer solution, the assembled biosensor was monitored in 3.0 mL of H_2O_2 (1.0 mM) solution partially containing phosphate buffer (PBS) (0.02 M, pH 7.4). Simultaneously, the continuous potential scanning was carried out on the working electrode for electrochemical measurements from −1.2 to 1.2 V with a scan rate of 200 mV/s. The ECL responses were monitored using an MPI-E electrochemiluminescence analyzer, and the voltage of the photomultiplier tube (PMT) was set at 800 V.

3. RESULTS AND DISCUSSION

3.1. Characterization of 3D-rGO@Au NPs. The morphology and structural properties of the synthesized 3D-

https://doi.org/10.1021/acsami.1c05368
ACS Appl. Mater. Interfaces 2021, 13, 25783−25791

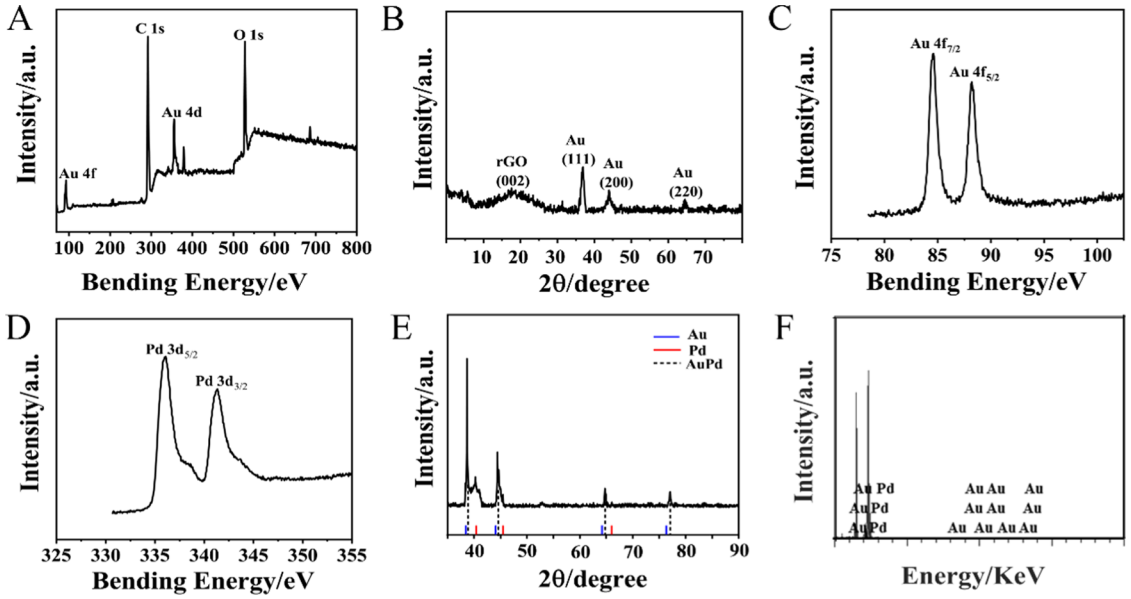

Figure 2. (A) XPS analysis of 3D-rGO@Au NPs. (B) XRD analysis of 3D-rGO@Au NPs. (C, D) XPS analysis of AuPd NPs. (E) XRD and (F) EDS analysis of AuPd NPs.

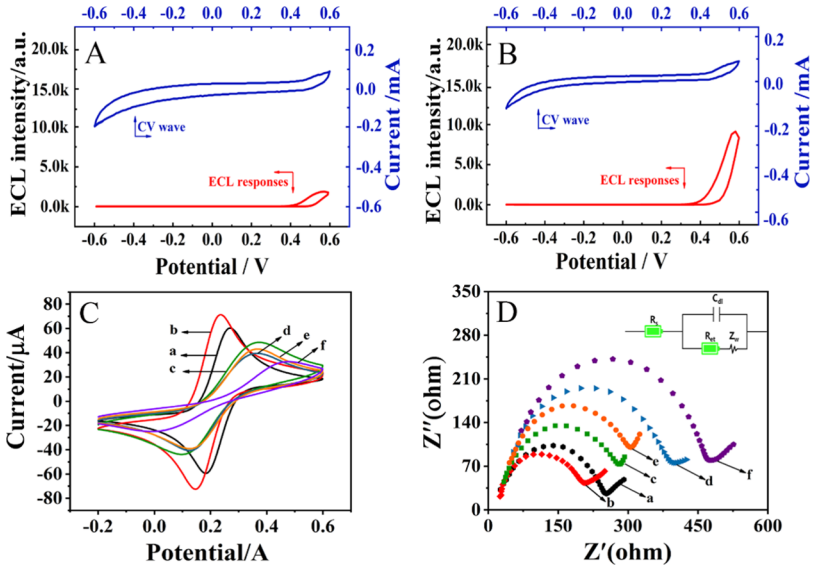

Figure 3. ECL−potential lineament (red line) and the peak current of corresponding CV curves (blue line) of (A) ABEI and (B) ABEI@AuPd NPs. (C) CV and (D) a different modified procedure of EIS in 5 mM $[Fe(CN)_6]^{3-/4-}$ containing 0.1 M KCl: (a) unmodified bare GCE, (b) 3D-rGO@Au NPs-GCE, (c) DNA swing arm/DNA3/3D-rGO@Au NPs-GCE, (d) MCH/DNA swing arm/DNA3/3D-rGO@Au NPs-GCE, (e) ABEI@AuPd NPs/MCH/DNA swing arm/DNA3/3D-rGO@Au NPs-GCE, and (f) miRNA-141/ABEI@AuPd NPs/MCH/DNA swing arm/DNA3/3D-rGO@Au NPs-GCE.

rGO@Au NPs were demonstrated by various techniques. The Au NPs were uniformly dispersed in wrinkles of 3D-rGO, which was investigated by the scanning electron microscopy (SEM) technique and transmission electron microscopy (TEM) technique, as displayed in Figure 1A,B. The X-ray photoelectron spectroscopy (XPS) results (Figure 2A) revealed a decrease of the peak intensity corresponding to the C−O group, indicating that a portion of the oxygen functional groups is reduced by sodium citrate and displaced by Au NPs. As shown in Figure 2B, the structure of the synthesized 3D-rGO@Au NPs was illustrated by X-ray diffraction (XRD) patterns. They had remarkable peaks at 2θ values of 37.8, 44.6, and 64.5°, which were assigned to the face-centered cubic (fcc) Au planes of (111), (200), and (220), respectively. The XRD spectrograms were consistent with the standard values of gold (JCPDS 04-0784), proving that Au NPs have been successfully germinated on 3D-rGO in situ, which is conducive to the subsequent stable loading of double-stranded DNA (dsDNA) and single-stranded DNA (ssDNA) on the GCE through the Au−S bond.

3.2. Characterization of AuPd NPs. In this work, as a multifunctional signal regulator, AuPd NPs were characterized by SEM (Figure 1C) and TEM (Figure 1D). The size and structure of AuPd NPs can be determined by SEM and TEM, which show a regular spherical shell with a solid core and many branched nanostructures. Especially on the basis of the high-

https://doi.org/10.1021/acsami.1c05368
ACS Appl. Mater. Interfaces 2021, 13, 25783−25791

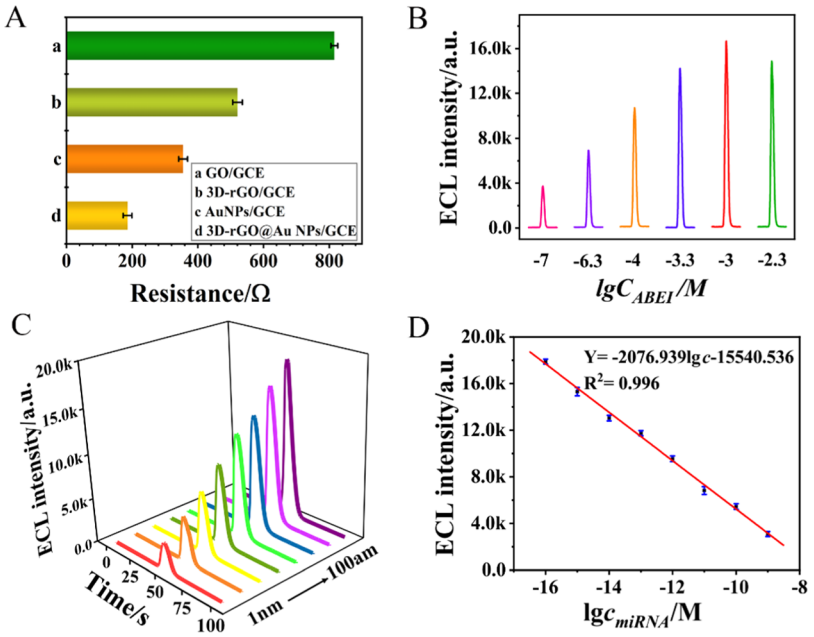

Figure 4. (A) Optimization of the electrical conductivity of GCE: (a) GO grows in the GCE region, (b) 3D-rGO grows in the GCE region, (c) Au NPs grow in the GCE region, and (d) 3D-rGO@Au NPs/GCE grows in the GCE region (error bars show S.D., n = 3). (B) Electrochemiluminescence responses of the as-synthesized biosensor with various modification concentrations of ABEI: 0.1 μM, 0.5 μM, 0.1 mM, 0.5 mM, 1 mM, and 5 mM, in PBS (0.1 M, pH 7.0) containing 1.0 mM H_2O_2. (C) ECL responses of the biosensor with various concentrations of miRNA-141: 100 aM, 1 fM, 10 fM, 100 fM, 1 pM, 10 pM, 100 pM, and 1 nM, under the condition of PBS (0.02 M, pH 7.4) containing 1.0 mM H_2O_2. (D) Curve of the ECL strength vs the logarithm of the miRNA-141 concentration (error bars show S.D., n = 3).

magnification TEM image, AuPd NPs were uniformly dispersed on porous spherical shells with a diameter of about 60 nm. As shown by XPS analysis and elemental verification (Figure 2C,D), not only were the characteristic peaks of the single Au 4f spectrum completely consistent with the database but the Pd 3d spectrum peaks also matched perfectly, which further confirms the presence of Au and Pd. In Figure 2E, the crystalline structure of AuPd NPs was analyzed on the pretext of XRD, and the results demonstrated that four reflection peaks appeared at 77.8, 64.8, 44.8, and 38.4° were evenly distributed between Pd (reference code 00-005-0681) and Au (reference code 00-004-0784). In addition, energy-dispersive X-ray spectroscopy (EDS) showed two sharp emission peaks of Au and Pd elements (Figure 2F), indicating that the elemental type and content of AuPd NPs were confirmed, and the composite was prepared successfully.

3.3. Performance and Mechanism of the Ternary ECL Biosensor. The corresponding ECL signal and the peak current of cyclic voltammetry (CV) curves of the ABEI and ABEI@AuPd NP-modified electrode were noted, for determining the ECL enhancement mechanism of AuPd NPs to ABEI. As shown in Figure 3A, the ECL signal and CV curves of the ABEI are demonstrated from −0.6 to 0.6 V, respectively. Distinctly, in the presence of individual ABEI, the ECL response showed minor fluctuations around 3552 au, which were associated with the partially reduced H_2O_2 at −0.26 V low currents. Nevertheless, after the ABEI@AuPd NPs were modified on the as-prepared electrode, the ECL response reached a new level of 18 352 au (Figure 3B), which was nearly 6 times higher than that of the nonmodified single ABEI.

The potential amplification mechanism is shown in Scheme 1C. H_2O_2 was decomposed to produce a large amount of $O_2^{\bullet-}$, due to the inherent oxidase-like catalytic activity of the AuPd NP alloy as a coreaction accelerator (reaction 1). Then, the as-obtained $O_2^{\bullet-}$ radical rapidly transformed into O_2 and OH^- due to its instability in aqueous solution (reaction 2). Furthermore, under alkaline conditions, the ground-state ABEI was electrochemically reduced to negatively charged radicals (noted as $ABEI^{\bullet-}$) (reaction 3). Then, $ABEI^{\bullet-}$ was further reacted with remaining $O_2^{\bullet-}$ to generate excited-state 4-aminophthalate anions (noted as $ABEI^{2-*}$) (reaction 4). Finally, light was emitted by $ABEI^{2-*}$ when it returned to the ground state (reaction 5). The corresponding equations are proposed as follows

$$H_2O_2 + e^- \xrightarrow{\text{AuPd NPs}} O_2^{\bullet-} + OH^{\bullet} \quad (1)$$

$$O_2^{\bullet-} + H_2O_2 \rightarrow O_2 + OH^{\bullet} + OH^- \quad (2)$$

$$ABEI + OH^- - e^- \rightarrow ABEI^{\bullet-} + H_2O \quad (3)$$

$$ABEI^{\bullet-} + O_2^{\bullet-} \rightarrow ABEI^{2-*} \quad (4)$$

$$ABEI^{2-*} \rightarrow ABEI^{2-} + hv \quad (5)$$

3.4. Electrochemiluminescence Characterization of the Biosensor. To determine the performance of the as-prepared biosensor, the electrode was progressively verified in the buffer containing PBS (pH 7.4, 0.02 M) and 1.0 mM H_2O_2 and studied by CV scan curves. As depicted in Figure 3C, a well-defined redox peak has emerged in the naked GCE (Figure 3C, curve a). When 3D-rGO@Au NPs were decorated on the electrode, the CV curve increased significantly (Figure 3C, curve b), which proved that 3D-rGO@Au NPs had high surface activity and good conductivity. However, when such nonconductive macromolecular oligonucleotides DNA swing arms were incubated on the electrode, their aimless walking made the rate of electron transfer on the electrode extremely limited, resulting in a sharp decrease in the redox peak (Figure

https://doi.org/10.1021/acsami.1c05368
ACS Appl. Mater. Interfaces 2021, 13, 25783−25791

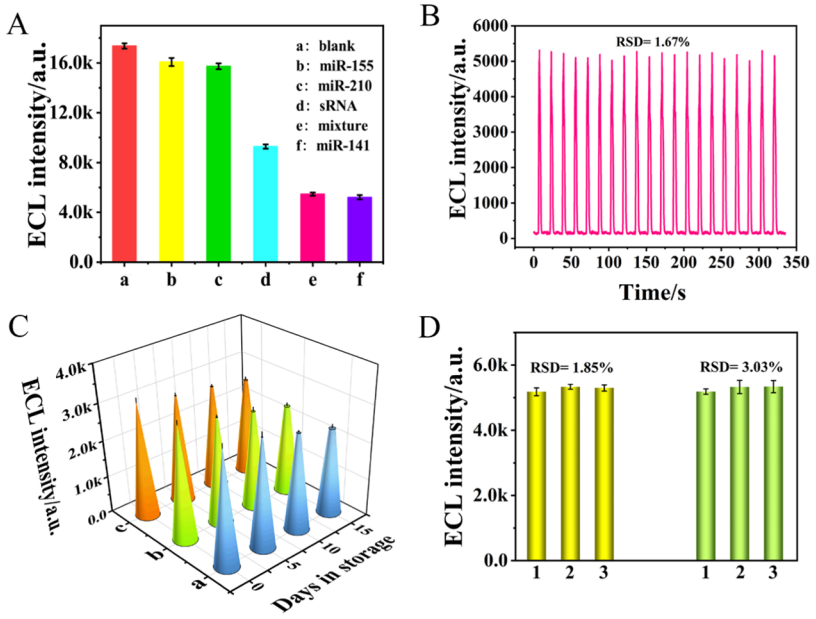

Figure 5. (A) Specificity of the as-proposed ECL biosensor for various interfering substrates: (a) blank (0 nM miRNA-141), (b) miRNA-155 (100 nM), (c) miRNA-210 (100 nM), (d) sRNA (100 nM), (e) the mixture RNA (100 nM), and (f) miRNA-141 (1 nM), in PBS (0.02 M, pH 7.4) containing 1.0 mM H_2O_2 (error bars show S.D., n = 3). (B) Stability of the as-proposed biosensor under consecutive cyclic potential scanning for 20 cycles and (C) for various storage conditions: (a) at room temperature, (b) in a refrigerator, and (c) in a freezer (error bars show S.D., n = 3). (D) Reproducibility of the GCE-ECL biosensor in three parallel intra-assays and interassays (error bars show S.D., n = 3).

3C, curve c). Due to the fact that the active sites on the electrode were accurately sealed by the organic polymer compound MCH, the peak current decreased further (Figure 3C, curve d). Expectedly, the transfer rate of electrons was accelerated and the peak current was significantly enhanced, when AuPd NPs with catalytic activity were grown on the obtained GCE (Figure 3C, curve e). Finally, in the presence of miRNA-141, the steric hindrance of the modified electrode increased, leading the peak value of redox current to slightly decrease again (Figure 3C, curve f). Thus, the reasonable variations in the CV peak current can justify the successful assembly of the biosensor.

As a common method of electrode process dynamics calculation, electrochemical impedance spectroscopy (EIS) has made a great contribution to checking the manufacturing procedure of the biosensor. Figure 3D shows the charge-transfer resistance (R_{et}) of different preparation steps, and the illustration is the relevant equivalent circuit. In the high-frequency field, a semicircle with a larger radius of the bare GCE was detected (Figure 3D, curved a). For 3D-rGO@Au NPs/GCE, a comparatively small semicircle was exhibited in the impedance spectrum (Figure 3D, curve b), which testified that 3D-rGO@Au NPs had favorable electric conductivity. Nevertheless, when the DNA swing arm was incubated with the 3D-rGO@Au NPs/GCE, it could be inferred that the R_{et} increased due to the insulativity of the nucleic acids (Figure 3D, curve c). After being modified by MCH, the R_{et} was significantly increased again (Figure 3D, curve d) on account of the nonconductivity of the organic molecule further hindered the current in the high-frequency region. Nevertheless, under the influence of the superior electrical conductivity and high-speed charge-transfer of AuPd NPs, the R_{et} would be drastically reduced in the presence of ABEl@AuPd NPs (Figure 3D, curve e). Furthermore, after incubation with miRNA-141, the ABEl@AuPd NPs-DNA3 slips away gradually under the degradation of T7 Exo, which led to the sharp increase of the R_{et} again, and thus reaching the maximum (Figure 3D, curve f).

3.5. Detection of miRNA-141. The electrode material and luminescent substance concentration were optimized (Figure 4A,B). Under the optimal conditions (see the Supporting Information for further details), the ECL response was detected by changing the concentration of miRNA-141. As depicted in Figure 4C, with the increase of the miRNA-141 concentration, more ABEI@AuPd NPs left the electrode interface, resulting in the disappearance of the redox reaction effect and the weakening of the ECL signal response. In Figure 4D, the ECL signal response appeared linearly decreased, with an increase in the logarithm concentration of miRNA-141 in the range from 100 aM to 1 nM. The regression equation was $I = -2076.939 \lg c_{miRNA} - 15540.536$ (R^2 = 0.996), and the limit of detection was evaluated to be 31.9 aM at a signal-to-noise ratio of 3, which confirmed the biosensor has the advantages of wide linear detection range and low detection limit in this work. The reason for the low detection limit was the intensive loading capacity of ABEI and the violently catalytic performance effect of AuPd NPs (performance of miRNA detection contrasted with other works, see Supporting Information Table S1).

3.6. Selectivity, Stability, and Reproducibility of the ECL Biosensor. To demonstrate the selectivity of the ECL biosensor toward miRNA-141, different ECL signal responses of the biosensor with various RNA sequences including miRNA-141, miRNA-155, miRNA-210, and sRNA were performed under the same conditions. As depicted in Figure 5A, the results of miRNA-155 and miRNA-210 were almost unchanged, while the results of miRNA-141 significantly decreased. As for sRNA, although the ECL response also decreased, it was much lower than that of miRNA-141. These comparison results convincingly demonstrated that the as-prepared ECL biosensor was highly selective.

https://doi.org/10.1021/acsami.1c05368
ACS Appl. Mater. Interfaces 2021, 13, 25783−25791

Under 20 consecutive cyclic potential scanning cycles, the ECL intensity of the biosensor showed no significant fluctuation (relative standard deviation (RSD) = 1.67%) in the presence of 100 pM miRNA-141 (Figure 5B). As depicted in Figure 5C, when the biosensor was kept at 4 °C, it maintained 98.65% in the first 5 days, then reduced by 3.8% in the next 10 days, and maintained 94.85% of the initial reaction after 15 days, indicating that the ECL intensity had excellent stability for the detection of miRNA-141.

Moreover, the reproducibility of the ECL biosensor was evaluated by intra-assay and interassay differences, and the corresponding RSDs (S/N = 3) were determined as 1.85 and 3.03%, respectively (Figure 5D). Therefore, the reproducibility of the proposed biosensor was satisfactory.

4. CONCLUSIONS

In summary, a ternary ECL biosensor based on DNA walkers was successfully developed for the ultrasensitive determination of miRNA-141 with a 3D-rGO@Au NP platform and AuPd NPs as a coreaction accelerator. We prepared 3D-rGO as the electrode material, which vigorously multiplied the prototypical specific surface area and provided convenience for the in situ growth of Au NPs, thus double promoting the electron transfer rate. AuPd NPs as a coreaction accelerator tremendously boosted the catalytic efficiency of H_2O_2, causing an enormous amplified ECL signal. Moreover, with DNA walker amplification, the proposed biosensor can achieve the circulation of the target and the accumulation of the signal simultaneously. Imitating the originality of nature, changing from an ordinary single-mechanism-driven biosensor to a multiple-mechanism-driven one would open up a promising route toward the clinical detection of different biomolecules.

■ ASSOCIATED CONTENT

Supporting Information

The Supporting Information is available free of charge at https://pubs.acs.org/doi/10.1021/acsami.1c05368.

Materials and reagents; apparatus; and optimization of experimental conditions (PDF)

■ AUTHOR INFORMATION

Corresponding Author

Shenguang Ge − *Institute for Advanced Interdisciplinary Research, University of Jinan, Jinan 250022, P. R. China;* orcid.org/0000-0002-0537-6491; Phone: +86-531-82767161; Email: chm_gesg@163.com

Authors

Qian Wang − *Institute for Advanced Interdisciplinary Research, University of Jinan, Jinan 250022, P. R. China; School of Chemistry and Chemical Engineering, University of Jinan, Jinan 250022, P. R. China*

Yaqi Liu − *Institute for Advanced Interdisciplinary Research, University of Jinan, Jinan 250022, P. R. China*

Xuefeng Wang − *Institute for Advanced Interdisciplinary Research, University of Jinan, Jinan 250022, P. R. China*

Fengyi Wang − *Institute for Advanced Interdisciplinary Research, University of Jinan, Jinan 250022, P. R. China*

Lina Zhang − *Shandong Provincial Key Laboratory of Preparation and Measurement of Building Materials, University of Jinan, Jinan 250022, P. R. China*

Jinghua Yu − *School of Chemistry and Chemical Engineering, University of Jinan, Jinan 250022, P. R. China;* orcid.org/0000-0001-5043-0322

Complete contact information is available at: https://pubs.acs.org/10.1021/acsami.1c05368

Author Contributions

‖Q.W. and Y.L. contributed equally to this work.

Notes

The authors declare no competing financial interest.

■ ACKNOWLEDGMENTS

This work was supported by the National Natural Science Foundation of China (22074053, 21775055, and 21874055), the Excellent Youth Innovation Team in Universities of Shandong (2019KJC016), The Project of "20 Items of University" of Jinan (2020GXRC047 and 2018GXRC001), the Taishan Scholars program, and the Case-by-Case Project for Top Outstanding Talents of Jinan.

■ REFERENCES

(1) Kang, Q.; He, M.; Chen, B.; Xiao, G.; Hu, B. MNAzyme-Catalyzed Amplification Assay with Lanthanide Tags for the Simultaneous Detection of Multiple MicroRNAs by Inductively Coupled Plasma-Mass Spectrometry. *Anal. Chem.* **2021**, *93*, 737−744.

(2) Cardoso, A. R.; Moreira, F. T. C.; Fernandes, R.; Sales, M. G. F. Novel and Simple Electrochemical Biosensor Monitoring Attomolar Levels of miRNA-155 in Breast Cancer. *Biosens. Bioelectron.* **2016**, *80*, 621−630.

(3) Chen, Y.; Gao, D. Y.; Huang, L. In Vivo Delivery of miRNAs for Cancer Therapy: Challenges and Strategies. *Adv. Drug Delivery Rev.* **2015**, *81*, 128−141.

(4) Wang, S.; Zhang, J.; Wang, Y.; Chen, M. Hyaluronic Acid-Coated PEI-PLGA Nanoparticles Mediated Co-Delivery of Doxorubicin and miR-542-3p for Triple Negative Breast Cancer Therapy. *Nanomedicine* **2016**, *12*, 411−420.

(5) Tang, W.; Wan, S.; Yang, Z.; Teschendorff, A. E.; Zou, Q. Tumor Origin Detection With Tissue-Specific miRNA and DNA Methylation Markers. *Bioinformatics* **2018**, *34*, 398−406.

(6) Chen, J. X.; Zhuo, Y.; Peng, X.; Chai, Y. Q.; Yuan, R.; Liang, W. B. A Dynamic DNA Machine via Free Walker Movement on Lipid Bilayer for Ultrasensitive Electrochemiluminescent Bioassay. *Anal. Chem.* **2019**, *91*, 14125−14132.

(7) Peng, X.; Yan, H.; Wu, Z.; Wen, W.; Zhang, X.; Wang, S. Magnetic Nanobeads and De Novo Growth of Electroactive Polymers for Ultrasensitive MicroRNA Detection at the Cellular Level. *Anal. Chem.* **2021**, *93*, 902−910.

(8) Oudeng, G.; Au, M.; Shi, J.; Wen, C.; Yang, M. One-Step in Situ Detection of miRNA-21 Expression in Single Cancer Cells Based on Biofunctionalized MoS2 Nanosheets. *ACS Appl. Mater. Interfaces* **2018**, *10*, 350−360.

(9) Xiao, F.; Liu, J.; Guo, Q.; Du, Z.; Li, H.; Sun, C.; Du, W. Dual-Signal Amplification Strategy for Sensitive MicroRNA Detection Based on Rolling Circle Amplification and Enzymatic Repairing Amplification. *ACS Omega* **2020**, *5*, 32738−32743.

(10) Honcharenko, D.; Druceikaite, K.; Honcharenko, M.; Bollmark, M.; Tedebark, U.; Strömberg, R. New Alkyne and Amine Linkers for Versatile Multiple Conjugation of Oligonucleotides. *ACS Omega* **2021**, *6*, 579−593.

(11) Zhao, Q.; Piao, J.; Peng, W.; Wang, Y.; Zhang, B.; Gong, X.; Chang, J. Simple and Sensitive Quantification of MicroRNAs via PS@Au Microspheres-Based DNA Probes and DSN-Assisted Signal Amplification Platform. *ACS Appl. Mater. Interfaces* **2018**, *10*, 3324−3332.

(12) Dong, H.; Lei, J.; Ding, L.; Wen, Y.; Ju, H.; Zhang, X. MicroRNA: Function, Detection, and Bioanalysis. *Chem. Rev.* **2013**, *113*, 6207−6233.
(13) Yuan, P.; Mao, X.; Liew, S. S.; Wu, S.; Huang, Y.; Li, L.; Yao, S. Q. Versatile Multiplex Endogenous RNA Detection with Simultaneous Signal Normalization Using Mesoporous Silica Nanoquenchers. *ACS Appl. Mater. Interfaces* **2020**, *12*, 57695−57709.
(14) Pikula, M.; Ali, M. M.; Filipe, C.; Hoare, T. Single-Step Printable Hydrogel Microarray Integrating Long-Chain DNA for the Discriminative and Size-Specific Sensing of Nucleic Acids. *ACS Appl. Mater. Interfaces* **2021**, *13*, 2360−2370.
(15) Wang, H.; Wang, H.; Wu, Q.; Liang, M.; Liu, X.; Wang, F. A DNAzyme-Amplified DNA Circuit for Highly Accurate MicroRNA Detection and Intracellular Imaging. *Chem. Sci.* **2019**, *10*, 9597−9604.
(16) Zhou, W.; Tian, Y. F.; Yin, B. C.; Ye, B. C. Simultaneous Surface-Enhanced Raman Spectroscopy Detection of Multiplexed MicroRNA Biomarkers. *Anal. Chem.* **2017**, *89*, 6120−6128.
(17) Suhito, I. R.; Han, Y.; Ryu, Y. S.; Son, H.; Kim, T. H. Autofluorescence-Raman Mapping Integration Analysis for Ultra-Fast Label-Free Monitoring of Adipogenic Differentiation of Stem Cells. *Biosens. Bioelectron.* **2021**, *178*, No. 113018.
(18) Xu, S.; Chang, Y.; Wu, Z.; Li, Y.; Yuan, R.; Chai, Y. One DNA Circle Capture Probe with Multiple Target Recognition Domains for Simultaneous Electrochemical Detection of miRNA-21 and miRNA-155. *Biosens. Bioelectron.* **2020**, *149*, No. 111848.
(19) Chen, T.; Chen, Y.; Chen, H.; Zhang, F.; Zhang, Q.; Chen, G.; Zhu, X. Dual-Enzyme-Propelled Unbounded DNA Walking Nanomachine for Intracellular Imaging of Lowly Expressed MicroRNA. *Nano Res.* **2019**, *12*, 1055−1060.
(20) Oishi, M.; Saito, K. Simple Single-Legged DNA Walkers at Diffusion-Limited Nanointerfaces of Gold Nanoparticles Driven by a DNA Circuit Mechanism. *ACS Nano* **2020**, *14*, 3477−3489.
(21) Liu, C.; Hu, Y.; Pan, Q.; Yi, J.; Zhang, J.; He, M.; He, M.; Chen, T.; Chu, X. A MicroRNA-Triggered Self-Powered DNAzyme Walker Operating in Living Cells. *Biosens. Bioelectron.* **2019**, *136*, 31−37.
(22) Cai, R.; Zhang, S.; Chen, L.; Li, M.; Zhang, Y.; Zhou, N. Self-Assembled DNA Nanoflowers Triggered by a DNA Walker for Highly Sensitive Electrochemical Detection of Staphylococcus Aureus. *ACS Appl. Mater. Interfaces* **2021**, *13*, 4905−4914.
(23) Wang, T.; Zhou, L.; Bai, S.; Zhang, Z.; Li, J.; Jing, X.; Xie, G. Ultraspecific Electrochemical DNA Biosensor by Coupling Spontaneous Cascade DNA Branch Migration and Dual-Signaling Sensing Strategy. *Biosens. Bioelectron.* **2016**, *78*, 464−470.
(24) Yan, Y.; Qiao, Z.; Hai, X.; Song, W.; Bi, S. Versatile Electrochemical Biosensor Based on Bi-Enzyme Cascade Biocatalysis Spatially Regulated by DNA Architecture. *Biosens. Bioelectron.* **2021**, *174*, No. 112827.
(25) Zhang, H.; Xu, X.; Jiang, W. An Interparticle Relatively Motional DNA Walker and Its Sensing Application. *Chem. Sci.* **2020**, *11*, 7415−7423.
(26) Zhang, K.; Wang, K.; Huang, Y.; Zhu, X.; Xie, M.; Wang, J. Sensitive Detection of Cytokine in Complex Biological Samples by Using MB Track Mediated DNA Walker and Nicking Enzyme Assisted Signal Amplification Method Combined Biosensor. *Talanta* **2018**, *189*, 122−128.
(27) Yang, X.; Tang, Y.; Mason, S. D.; Chen, J.; Li, F. Enzyme-Powered Three-Dimensional DNA Nanomachine for DNA Walking, Payload Release, and Biosensing. *ACS Nano* **2016**, *10*, 2324−2330.
(28) Zhang, P.; Jiang, J.; Yuan, R.; Zhuo, Y.; Chai, Y. Highly Ordered and Field-Free 3D DNA Nanostructure: The Next Generation of DNA Nanomachine for Rapid Single-Step Sensing. *J. Am. Chem. Soc.* **2018**, *140*, 9361−9364.
(29) Yang, J.; Xia, Q.; Guo, L.; Luo, F.; Dong, Y.; Qiu, B.; Lin, Z. A highly Sensitive Signal-On Biosensor for MicroRNA 142-3p Based on the Quenching of Ru(bpy)3(2+)-TPA Electrochemiluminescence by Carbon Dots and Duplex Specific Nuclease-Assisted Target Recycling Amplification. *Chem. Commun.* **2020**, *56*, 6692−6695.
(30) Gou, L.; Sheng, Y.; Peng, Q.; Ling, J.; Yue, H.; Chen, F.; Tang, H. Ternary Nanocube-based "Off-On" Blinking-Type Electrochemiluminescence Towards Enzyme-Free Detection of Hepatitis B Virus (HBV)-Related DNA. *Sens. Actuators, B* **2020**, *312*, No. 127987.
(31) Wang, L.; Jiang, M. H.; Chai, Y. Q.; Yuan, R.; Zhuo, Y. Intense Electrochemiluminescence from an Organic Microcrystal Accelerated H2O2-Free Luminol System for MicroRNA Detection. *Chem. Commun.* **2020**, *56*, 9000−9003.
(32) Wang, H. F.; Ma, R. N.; Sun, F.; Jia, L. P.; Zhang, W.; Shang, L.; Xue, Q. W.; Jia, W. L.; Wang, H. S. A Versatile Label-Free Electrochemical Biosensor for Circulating Tumor DNA Based on Dual Enzyme Assisted Multiple Amplification Strategy. *Biosens. Bioelectron.* **2018**, *122*, 224−230.
(33) Xia, L. Y.; Li, M. J.; Wang, H. J.; Yuan, R.; Chai, Y. Q. Novel Single-Enzyme-Assisted Dual Recycle Amplification Strategy for Sensitive Photoelectrochemical MicroRNA Assay. *Anal. Chem.* **2020**, *92*, 14550−14557.
(34) Tian, L.; Qi, J.; Ma, X.; Wang, X.; Yao, C.; Song, W.; Wang, Y. A Facile DNA Strand Displacement Reaction Sensing Strategy of Electrochemical Biosensor Based on N-Carboxymethyl Chitosan/Molybdenum Carbide Nanocomposite for MicroRNA-21 Detection. *Biosens. Bioelectron.* **2018**, *122*, 43−50.
(35) Yuan, Y.; Li, X.; Chen, A. Y.; Wang, H. J.; Chai, Y. Q.; Yuan, R. Highly-Efficient Luminol Immobilization Approach and Exponential Strand Displacement Reaction Based Electrochemiluminescent Strategy for Monitoring MicroRNA Expression in Cell. *Biosens. Bioelectron.* **2019**, *132*, 62−67.
(36) Lei, Y. M.; Zhuo, Y.; Guo, M. L.; Chai, Y. Q.; Yuan, R. Pore Confinement-Enhanced Electrochemiluminescence on SnO2 Nanocrystal Xerogel with NO3(-) As Co-Reactant and Its Application in Facile and Sensitive Bioanalysis. *Anal. Chem.* **2020**, *92*, 2839−2846.
(37) Nie, Y.; Tao, X.; Zhou, Y.; Yuan, X.; Zhuo, Y.; Chai, Y. Q.; Yuan, R. Kill Three Birds with One Stone: Poly (3,4-Ethylenedioxythiophene)-Hosted Ag Nanoclusters with Boosted Cathodic Electrochemiluminescence for Biosensing Application. *Anal. Chem.* **2021**, *93*, 1120−1125.
(38) Wang, Z.; Tang, Y.; Fu, X.; Wang, J.; Peng, Z.; Zhang, L.; Huang, J. In Situ Imaging Polysulfides Electrochemistry of Li-S Batteries in a Hollow Carbon Nanotubule Wet Electrochemical Cell. *ACS Appl. Mater. Interfaces* **2020**, *12*, 55971−55981.
(39) Peng, H.; Huang, Z.; Wu, W.; Liu, M.; Huang, K.; Yang, Y.; Deng, H.; Xia, X.; Chen, W. Versatile High-Performance Electrochemiluminescence ELISA Platform Based on a Gold Nanocluster Probe. *ACS Appl. Mater. Interfaces* **2019**, *11*, 24812−24819.
(40) Pan, F.; Zhang, Y.; Yuan, Z.; Lu, C. Sensitive and Selective Carmine Acid Detection Based on Chemiluminescence Quenching of Layer Doubled Hydroxide-Luminol-H2O2 System. *ACS Omega* **2018**, *3*, 18836−18842.
(41) Xiong, S.; Yin, S.; Wang, Y.; Kong, Z.; Lan, J.; Zhang, R.; Gong, M.; Wu, B.; Chu, J.; Wang, X. Organic/Inorganic Electrochromic Nanocomposites with Various Interfacial Interactions: A review. *Mater. Sci. Eng., B* **2017**, *221*, 41−53.
(42) Zhang, N.; Shi, X. M.; Guo, H. Q.; Zhao, X. Z.; Zhao, W. W.; Xu, J. J.; Chen, H. Y. Gold Nanoparticle Couples with Entropy-Driven Toehold-Mediated DNA Strand Displacement Reaction on Magnetic Beads: Toward Ultrasensitive Energy-Transfer- Based Photoelectrochemical Detection of miRNA-141 in Real Blood Sample. *Anal. Chem.* **2018**, *90*, 11892−11898.
(43) Hu, G. B.; Xiong, C. Y.; Liang, W. B.; Zeng, X. S.; Xu, H. L.; Yang, Y.; Yao, L. Y.; Yuan, R.; Xiao, D. R. Highly Stable Mesoporous Luminescence-Functionalized MOF with Excellent Electrochemiluminescence Property for Ultrasensitive Immunosensor Construction. *ACS Appl. Mater. Interfaces* **2018**, *10*, 15913−15919.
(44) Yadav, J.; Liang, Q.; Pan, S. Electrogenerated Chemiluminescence and Spectroelectrochemistry Characteristics of Blue Photoluminescence Perovskite Quantum Dots. *ACS Appl. Mater. Interfaces* **2020**, *12*, 27443−27452.
(45) Yang, L.; Xue, J.; Jia, Y.; Zhang, Y.; Wu, D.; Ma, H.; Wei, Q.; Ju, H. Construction of Well-Ordered Electrochemiluminescence Sensing Interface Using Peptide-Based Specific Antibody Immobilizer and N-(Aminobutyl)-N-(Ethylisoluminol) Functionalized Ferritin as Signal

Indicator for Procalcitonin Analysis. *Biosens. Bioelectron.* **2019**, *142*, 111562.
(46) Liu, Y.; Zhang, J.; Tian, J.; Fan, X.; Geng, H.; Cheng, Y. Multiplex Detection of MicroRNAs by Combining Molecular Beacon Probes with T7 Exonuclease-Assisted Cyclic Amplification Reaction. *Anal. Bioanal. Chem.* **2017**, *409*, 107−114.
(47) Wu, H.; Wu, J.; Liu, Y.; Wang, H.; Zou, P. Target-Triggered and T7 Exonuclease-Assisted Cascade Recycling Amplification Strategy for Label-Free and Ultrasensitive Fluorescence Detection of Aflatoxin B1. *Sens. Actuators, B* **2020**, *321*, No. 128599.
(48) Liu, J. L.; Jiang, J.; Zhang, J. Q.; Chai, Y. Q.; Xiao, Q.; Yuan, R. The Combination of Ternary Electrochemiluminescence System of g-C3N4 Nanosheet/ TEA/Cu@Cu2O and G-quadruplex-Driven Regeneration Strategy for Ultrasensitive Bioanalysis. *Biosens. Bioelectron.* **2020**, *152*, No. 112006.
(49) Yun, W.; Zhong, H.; Zheng, S.; Wang, R.; Yang, L. Simple, One-Step and Amplified Hg2+ Detection Strategy Based on DNAzyme Motor. *Sens. Actuators, B* **2018**, *277*, 456−461.
(50) Li, D.; Xu, Y.; Fan, L.; Shen, B.; Ding, X.; Yuan, R.; Li, X.; Chen, W. Target-Driven Rolling Walker Based Electrochemical Biosensor for Ultrasensitive Detection of Circulating Tumor DNA Using Doxorubicin@Tetrahedron-Au Tags. *Biosens. Bioelectron.* **2020**, *148*, No. 111826.
(51) Yang, G.; Yang, B.; Mu, W.; Ge, Y.; Cai, Y.; Yao, Z.; Ma, Z.; Zhang, Y. M.; Zhang, S. X. A Transparent Multidimensional Electrode with Indium Tin Oxide Nanofibers and Gold Nanoparticles for Bistable Electrochromic Devices. *ACS Appl. Mater. Interfaces* **2020**, *12*, 27453−27460.

https://doi.org/10.1021/acsami.1c05368
ACS Appl. Mater. Interfaces 2021, 13, 25783−25791